Geophysical Journal International

Geophys. J. Int. (2019) **217,** 389–404
Advance Access publication 2019 January 15
GJI Seismology

doi: 10.1093/gji/ggz021

Comparison of high- and low-frequency signal sources for very-long-period seismic events at Asama volcano, Japan

Yuta Maeda [1], Minoru Takeo [2] and Ryunosuke Kazahaya [3]

[1] *Graduate School of Environmental Studies, Nagoya University, Furo-cho, Chikusa-ku, Nagoya, Aichi* 464–8601, *Japan. E-mail: maeda@seis.nagoya-u.ac.jp*
[2] *Earthquake Research Institute, The University of Tokyo, Tokyo 113-0032, Japan*
[3] *Geological Survey of Japan, The National Institute of Advanced Industrial Science and Technology, Tsukuba 305-8567, Japan*

Accepted 2019 January 11. Received 2019 January 9; in original form 2018 July 13

SUMMARY

Very-long-period (VLP) seismic events at Asama volcano in central Japan are characterized by a transient signal of 10–20 s duration. Associated with the transient motion, a high-frequency (HF) oscillation within the 5–10 Hz band is observed. We investigated the location and size of the oscillation source in the HF band (HF source) using an amplitude source location method and compared our results with those for the VLP band (VLP source) deduced in our previous waveform inversion study. We analysed 1437 VLP events recorded during an intense observation campaign during 2008–2009, and additional 571 events surrounding an eruptive activity in 2015 (including a VLP event that immediately preceded an eruption). The HF source locations of most events were deeper than the VLP source locations by ∼150 m, although there was almost no time lag between the signals. This suggests a strong connection between the two sources, with one source immediately responding to the other. The eruptive VLP event had an HF source location close to normal VLP events but had a greater event size. We surmise that the HF signal is caused by an inflow of volcanic gas from depth into a semi-vertical crack-like cavity (as imaged in our previous waveform inversion study), and the VLP signal is caused by resultant inflation of the same cavity. The centroid of inflation (VLP source) is near the roof of the cavity, where gas accumulates, whereas the HF oscillation is emitted more intensely from lower and narrower portions of the cavity. This results in source depth differences between the two signal bands. In this model, the inflation rate of the cavity is controlled by the volume flux of the gas inflow, producing similar temporal variations between the VLP and HF signals. According to this model, the eruptive VLP is associated with a greater amount of gas inflow and accumulation, which likely played a key role in the eruption.

Key words: Earthquake source observations; Volcano seismology; Eruption mechanisms and flow emplacement; Explosive volcanism; Volcano monitoring.

1 INTRODUCTION

Movements and volume changes of shallow volcanic fluids markedly affect the occurrence and style of eruptions (e.g. Sparks 2003). Such fluid behaviour could be monitored via seismic observations, especially of very-long-period (VLP) seismic events that have dominant periods of 2–100 s (Chouet & Matoza 2013). Over the past two decades, waveform inversion has been used extensively to study source mechanisms of VLP events. Study results reveal that VLP events may be caused by movements and volume changes of shallow volcanic fluids (e.g. Ohminato *et al.* 1998; Chouet *et al.* 2005). This interpretation was supported by analogue experiments (e.g. James *et al.* 2006).

Some VLP events are associated with high-frequency (HF) oscillations, such as in the cases of Merapi in Indonesia (Hidayat *et al.* 2002), Stromboli in Italy (Chouet *et al.* 2003) and Ontake in Japan (Nakamichi *et al.* 2009). HF oscillations may contain additional information on the source processes of VLP events. For example, Ohminato (2006) analysed repetitive VLP events at Satsuma-Iwojima volcano in Japan, by waveform inversion in the VLP band and an identification of increasing/decreasing stages of associated HF tremor amplitudes, which led him to model the source process of the events by a cycle of heating and vaporization of underground water within a cavity and escape of the gas from it through a constricted path. Jolly *et al.* (2017) analysed a seismic swarm at White Island in New Zealand, by locating VLP and long-

period (LP) band sources with a semblance method and an HF band source with a traveltime analysis. They pointed out that the VLP source was deeper than the LP and HF sources, which they interpreted by excitations of a magma carapace and an overlying hydrothermal system, respectively, caused by an upward migration of fluids.

Despite their importance, however, the HF oscillations associated with VLP events were filtered out in most previous studies because strong path effects make it difficult to perform analyses in the HF bands. Recent studies have shown that the amplitude source location (ASL) method (Battaglia & Aki 2003; Kumagai *et al.* 2010) is useful for locating the HF signal sources of volcanoes. This method assumes isotropic radiation of an *S* wave, produced by multiple scattering of the wave due to small-scale heterogeneities within the medium (Takemura *et al.* 2009; Kumagai *et al.* 2010; Morioka *et al.* 2017). It has been applied to volcano-tectonic, LP and explosive events, as well as tremors associated with magmatic and phreatic eruptions, underground dyke propagations and debris flows (e.g. Taisne *et al.* 2011; Kumagai *et al.* 2013; Ogiso & Yomogida 2015; Ogiso *et al.* 2015; Kurokawa *et al.* 2016; Caudron *et al.* 2018). It could potentially be applied to HF oscillations associated with VLP events to better constrain the source processes of VLP events.

The ASL method makes use of HF bands to locate sources of volcano-seismic signals. There are two advantages of adding ASL analyses for HF bands in VLP seismic studies. One is that it provides computational efficiency. Given that waveform inversion requires large amounts of computational time and memory, it is often the case that only several typical events are analysed, even when thousands of VLP events are observed. Using the ASL method, thousands of events can be analysed in a short time with a small amount of computational resources. The other advantage is that the short wavelengths of HF bands result in improved spatiotemporal resolution. Kumagai *et al.* (2011a) conducted combined analyses of waveform inversion of a VLP band and ASL analysis for an HF band for an explosion earthquake measured at Tungurahua volcano in Ecuador. The waveform inversion study suggested an isotropic source at 5-km depth, while the ASL analysis identified an upward-moving source during the event. Together, these data are consistent with a pressure wave propagating through a magma conduit being the trigger of the explosion. Their study clearly shows the advantage of combining the two analyses.

In this study, we applied an ASL analysis to HF oscillations associated with VLP events at Asama volcano in Japan. First, we describe the characteristics of VLP events at Asama volcano, before outlining our analysis method. We show the location and size of the HF source obtained from the ASL analysis and compare these data with those for the VLP source determined in our previous waveform inversion study (Maeda & Takeo 2011). On the basis of these results, we discuss a process that could simultaneously generate both HF and VLP signals.

2 VLP SEISMIC EVENTS AT ASAMA VOLCANO

Mount Asama (elevation: 2568 m) is one of the most active volcanoes in Japan. The volcano has a summit crater (diameter: 450 m; depth: 250 m) from which Vulcanian eruptions of andesitic magma have repeatedly occurred. Its recent activity involved moderate-sized Vulcanian eruptions in 2004, with smaller eruptions in 2008, 2009 and 2015.

Fig. 1 shows the seismometer network for Asama volcano. Station KMN was installed in 2011, while the other 16 permanent stations located within 5 km of the summit were all installed before the 2008 activity. We conducted a campaign with 10 additional broad-band seismometers within 1 km of the summit from 2008 September 22 to 2009 April 27.

This network has recorded VLP events at typical rates of several to several tens a day (Yamamoto *et al.* 2005; Kazahaya *et al.* 2015). The events are characterized by one-sided motion of around 10–20 s duration (Figs 2a and b). Maeda & Takeo (2011) performed waveform inversion of this transient motion using a frequency band below 1 Hz and obtained a source time function above the noise level from 0.002 to 0.1 Hz. The waveform inversion solution was an inflation–deflation source at 2150 m above sea level (approximately 150 m below the crater floor), beneath the northern part of the crater.

The VLP events at Asama volcano are associated with an HF oscillation of around 5–10 Hz (Figs 2c and d). The large amplitude portion (the main phase) of the oscillation within this HF band (5–10 Hz) is synchronized with transient motion in the VLP band (0.002–0.1 Hz). It is sometimes preceded by ∼20 s by another small HF oscillation, called the precursory phase. For example, a VLP event on 2008 October 28 consisted of a large HF oscillation from 17:18:10 to 17:18:30, preceded by a small oscillation from 17:17:50 to 17:18:10 (Fig. 2c).

A VLP event with an exceptionally long duration took place immediately before the eruption on 2015 June 16 (Figs 3a and b). Hereafter, we refer to this event as the eruptive VLP event. This event was also associated with an HF oscillation (Fig. 3c). Similar VLP events were recorded before three small eruptions in August 2008. Precursory increases of VLP seismicity before both 2008 and 2015 eruptions were reported (Kazahaya *et al.* 2015; Takeo *et al.* 2015).

3 ANALYSIS METHOD

Given that the HF oscillation was emergent, it was difficult to identify the onset time (Fig. 2c). Therefore, we investigated its source using the ASL method. We conducted the ASL analyses for the entire campaign period (from 2008 September 22 to 2009 April 27), as well as a 13-d period surrounding the eruptive activity in 2015 (from 2015 June 10 to 22, with eruptions on 2015 June 16 and 19; Japan Meteorological Agency 2015). We detected VLP events during these periods using an algorithm proposed by Kazahaya *et al.* (2015) and evaluated their data quality (Appendix A) to avoid analysing events having small signal-to-noise ratios or those contaminated by another earthquake. A total of 1437 events from the 2008–2009 campaign and additional 571 events in 2015 passed these criteria. We investigated the ASLs of the main phase for all these selected events. We also analysed the eruptive VLP event (Fig. 3), although it did not meet these data quality criteria due to the event duration longer than what was assumed in the criteria. We only analysed the precursory phase of events within the 2008–2009 period, given the dense campaign network available. A total of 152 events from this period satisfied our data quality criteria for the precursory phase.

We determined site amplification factors using the coda normalization method (Aki & Chouet 1975). We investigated these factors for two time periods independently; from 2008 September 30 to November 3 (2008 period) and from 2011 November 1 to December 31 (2011 period). We selected nine regional earthquakes

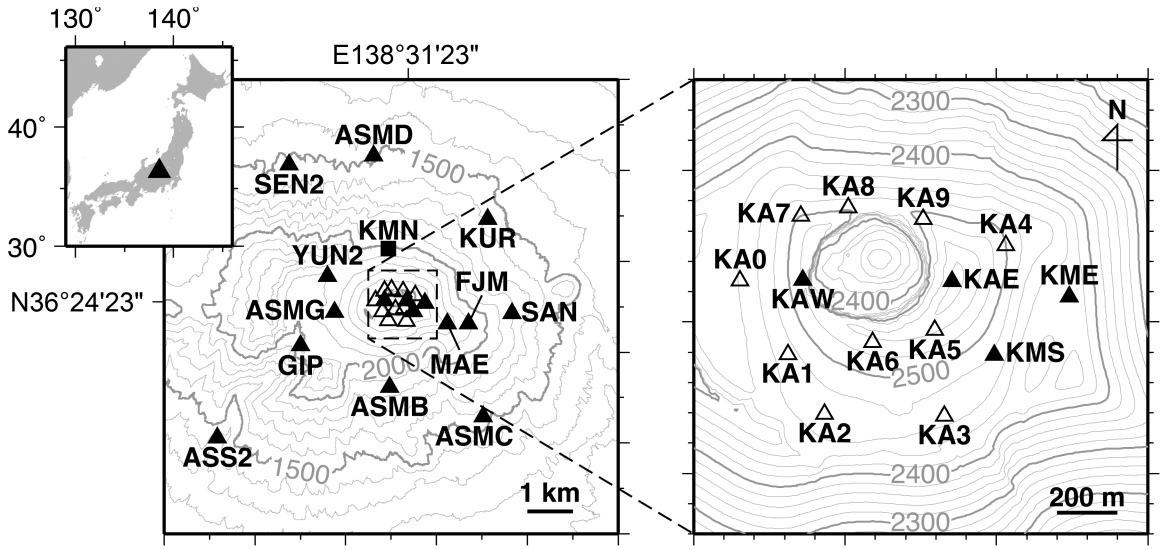

Figure 1. Station network at Asama volcano. Closed and open symbols represent permanent and campaign stations, respectively. Station KMN (square) was installed in 2011. Contours represent the topography. The inset indicates the location of Asama volcano at a regional scale.

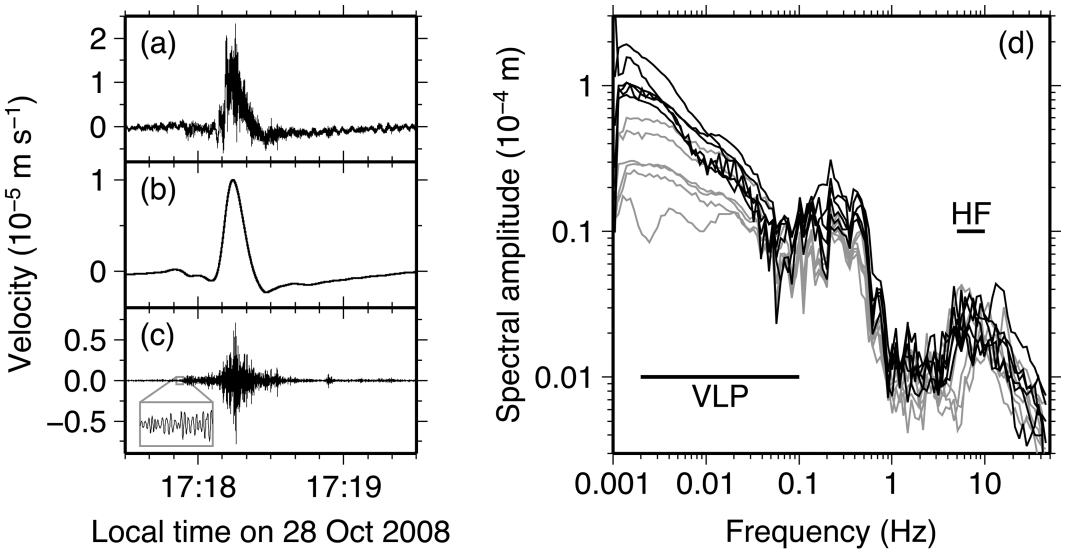

Figure 2. Waveforms and Fourier spectra for a very-long-period (VLP) event at 17:18:13 on 2008 October 28. (a–c) Vertical velocity waveforms at station KAE for raw, VLP (0.002–0.1 Hz) and high-frequency (HF; 5–10 Hz) bands which are defined based on waveform inversion (Maeda & Takeo 2011) and the amplitude source location (ASL) analysis (this study). The inset indicates an extension around the onset. (d) Smoothed Fourier amplitude spectra of the event at stations on the crater rim (KA5, KA6, KA8, KA9, KAE and KAW; black) and outside the rim but within 1 km of the crater (KA0-KA3, KME and KMS; grey). The bars represent the VLP and HF bands corresponding to panels (b) and (c), respectively. Instrument responses were deconvolved with a low-cut filter of 0.002 Hz.

during the 2008 period and 14 earthquakes during the 2011 period, with magnitudes greater than 2 and depths less than 100 km from a catalogue issued by Japan Meteorological Agency, taking into account signal-to-noise ratios and azimuthal distributions. We manually removed the traces significantly contaminated by local noise or some other non-earthquake signals. For each remaining trace of each earthquake, we calculated the envelope amplitude in a 5–10 Hz frequency band averaged over five 5-s-long time windows starting from twice the *S*-wave traveltime and overlapping by 2.5 s; in these time windows, the waveforms are dominated by the coda (Rautian & Khalturin 1978). The ratios of these coda amplitudes at individual stations to a reference station (MAE), averaged over all earthquakes, are regarded as the site amplification factors, which are shown in Table 1. The factors for the 2008 and 2011 periods showed similar values at each station.

In the ASL analysis of each event, we calculated vertical component envelope amplitudes in the HF band at individual stations, averaged over an analysis time window, the choice of which is described at the end of Section 3. We corrected for site amplification factors for the 2008 period (Table 1, left); for station KMN, we used the factors for the 2011 period (Table 1, right). We compared the corrected amplitude at each station with a value obtained using the following expression (Battaglia & Aki 2003; Kumagai *et al.* 2010):

$$v = S_0 \exp\left(-\pi f T/Q\right)/r,\ T = r/V_s, \tag{1}$$

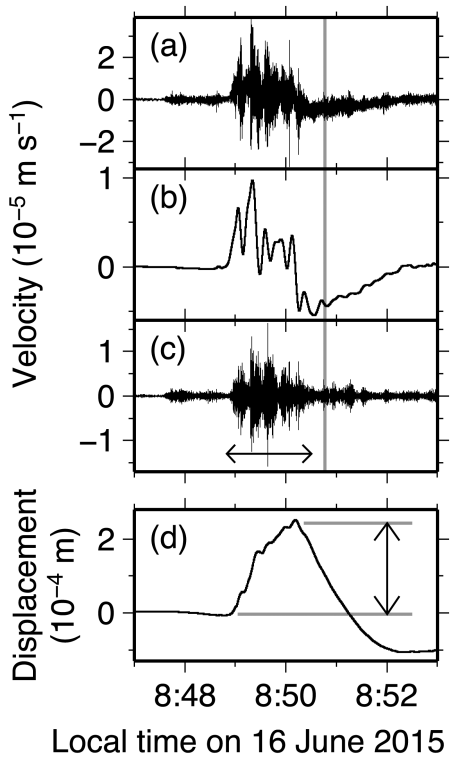

Figure 3. Waveforms and Fourier spectra for a VLP event at 8:49:20 on 2015 June 16 that immediately preceded an eruption (the eruptive VLP event). (a–c) Vertical velocity waveforms at station KAE for raw, VLP (0.002–0.1 Hz) and HF (5–10 Hz) bands. The grey bar represents the eruption onset time, estimated from an infrasonic record (Ohminato *et al.* 2015). The arrow in panel (c) shows the time window used in the ASL analysis. (d) A vertical displacement waveform at station KAE. The arrow represents our estimate of the displacement amplitude.

where r and T are the distance and traveltime from an assumed source location to the station, respectively; V_s and Q are the S-wave velocity and the quality factor of the medium, respectively; f is the central frequency of the analysis band (7.5 Hz); S_0 is a source amplitude that represents a theoretical amplitude at a unit distance from the source; and v is the velocity amplitude. We assumed a P-wave velocity $V_p = 2500$ m s^{-1} (Aoki *et al.* 2009; Maeda & Takeo 2011) and an S-wave velocity $V_s = V_p/\sqrt{3}$. We used $Q = 50$, which has been used in previous ASL studies of other volcanoes (Kumagai *et al.* 2013). We conducted a grid search for the assumed source location (at intervals of 50 m) to identify the location that best explained the observed amplitude distribution for each event. For each candidate source location, we derived the source amplitude S_0 using the least-squares fit of eq. (1) to the data. We examined the dependence of ASL results on assumed Q value and velocity structure using several different values of them (Appendix B). We also performed the ASL analysis using the theoretical amplitude expression of Morioka *et al.* (2017) and compared these results with those based on eq. (1) (Appendix C). Finally, we examined the effects of errors of the site amplification factors on the ASLs (Appendix D).

The source amplitude S_0 obtained using the ASL analysis could be considered a measure of the event size in the HF band (Kumagai *et al.* 2013). We compared S_0 values with the seismic moment and displacement amplitude, both considered as measures of the event size in the VLP band. Maeda & Takeo (2011) conducted a waveform inversion study of 23 selected VLP events during the 2008–2009 campaign and obtained stable estimates of the eigenvalues for the moment tensors for 19 of these events. The eigenvalue ratios of this subset were approximately M_1:M_2:M_3 = 5:3:2, where M_1, M_2 and M_3 are the largest, intermediate and smallest eigenvalues, respectively. Using this relationship, the seismic moment of each event in the VLP band was evaluated as $M_0 \sim (M_1/5 + M_2/3 + M_3/2)/3$. For 18 of these events, we investigated the source amplitude in the HF band (one event did not pass the data quality criteria for the ASL analysis because of contamination by another VLP event). In this way, we obtained both the source amplitude in the HF band and the seismic moment in the VLP band for these 18 VLP events. For the remaining events, although we did not have the seismic moment, we assumed that this quantity was proportional to the displacement amplitude in the VLP band in the near field. Theoretically, these quantities are proportional to each other in homogeneous infinite medium (*cf.* Aki & Richards 2002). At Asama volcano, the proportional relationship between them, given by

$$M_0\,(\mathrm{N\,m}) = 1.53 \times 10^{16} U_{\mathrm{KAE}}\,(\mathrm{m})\,, \qquad (2)$$

was investigated by Kazahaya *et al.* (2015), where U_{KAE} is the vertical displacement amplitude at station KAE. This relation was derived from waveform inversion results for the selected VLP events in October 2008 analysed by Maeda & Takeo (2011) and additional VLP events in June 2009 analysed by Kazahaya *et al.* (2011). This relation enabled us to compare the size estimates for the VLP events based on both HF and VLP bands, despite having no direct determination of the seismic moment for most of them. The waveforms at KAE have been used as a representative record for VLP seismic studies. This is because station KAE is one of the permanent stations that is the closest to the crater, has a flat response from 0.02 to 360 s and has been operating since 2007. To automatically compute U_{KAE} values for every event from the velocity waveform, we used the average value over an interval of 10–40 s before the event time as the baseline.

We report ASL results for a fixed 60 s window, covering the interval from 20 s before to 40 s after the event time, which includes the main phase of the HF oscillation (Fig. 2). We also tested a 10 s moving window with a 5 s overlap, as used in previous ASL studies (Kumagai *et al.* 2013). We found no systematic difference between the source locations, when using the 10 and 60 s windows, although the source amplitude for the 60 s window correlated better with the seismic moment. In our analysis of the precursory phase, we used a time window of 10–30 s before the event time. We took into account the traveltime from the assumed source to each station when calculating the observed HF amplitudes in these time windows.

In the case of the eruptive VLP event, which had an exceptionally long duration (Fig. 3), the 60 s window was not long enough to encompass the main phase. We manually determined that a 100 s window from 8:48:50 to 8:50:30 (Fig. 3c) was the appropriate interval for ASL analysis of this event. We used the interval from 8:47:10 to 7:47:20 to evaluate the noise level at each station. For the eruptive VLP event, the station KMN did not pass the data quality criteria (Appendix A) because the maximum amplitude was recorded during the later stages of the long-lasting signal than assumed in the criteria. Nevertheless, we used this station in our ASL analysis because it was essential to constrain the N–S source location. We also investigated the displacement amplitude of this event manually (Fig. 3d) because our automated baseline correction using a 10–40 s interval before the event resulted in the subtraction of some of the signals.

The time lags between the signals in the two frequency bands provided an additional constraint on the source processes of these

Table 1. Site amplification factors relative to station MAE for the 5–10 Hz frequency band in 2008 and 2011 periods, estimated from earthquakes shown in Figs 4(a) and (b), respectively.

Station[a]	Factor[b] (2008)	Factor[b] (2011)
ASMB	0.860217 ± 0.171495 (8)	0.955673 ± 0.203454 (14)
ASMC	1.157685 ± 0.128870 (6)	
ASMD	0.385381 ± 0.088623 (9)	
ASMG	0.389988 ± 0.069043 (9)	
ASS2	0.285422 ± 0.118086 (7)	
FJM	1.058188 ± 0.034310 (9)	1.256552 ± 0.182442 (12)
GIP	0.128999 ± 0.041468 (9)	0.173922 ± 0.062184 (14)
KA0	0.270507 ± 0.052621 (9)	
KA1	0.368157 ± 0.059776 (9)	
KA2	0.302654 ± 0.045607 (9)	
KA3	0.718062 ± 0.090880 (9)	
KA4	0.446550 ± 0.033439 (9)	
KA5	0.359157 ± 0.034661 (9)	
KA6	0.581637 ± 0.092333 (9)	
KA7	0.352131 ± 0.051119 (9)	
KA8	0.438836 ± 0.086155 (9)	
KA9	0.547960 ± 0.101293 (9)	
KAE	0.521147 ± 0.049200 (9)	0.490106 ± 0.102517 (14)
KAW	0.450797 ± 0.072102 (9)	0.404019 ± 0.046872 (13)
KME	0.828588 ± 0.060143 (9)	0.790972 ± 0.129957 (14)
KMN		0.503987 ± 0.128427 (14)
KMS	0.701210 ± 0.034540 (9)	0.647564 ± 0.116878 (14)
KUR	0.435702 ± 0.055562 (9)	0.447347 ± 0.091834 (14)
SAN	0.954542 ± 0.082768 (8)	1.040720 ± 0.230430 (14)
SEN2	0.488836 ± 0.231540 (7)	
YUN2	0.238670 ± 0.087947 (9)	0.321357 ± 0.088162 (14)

[a]Locations of these stations are shown in Fig. 1.
[b]The numbers of earthquakes used are shown in the parentheses.

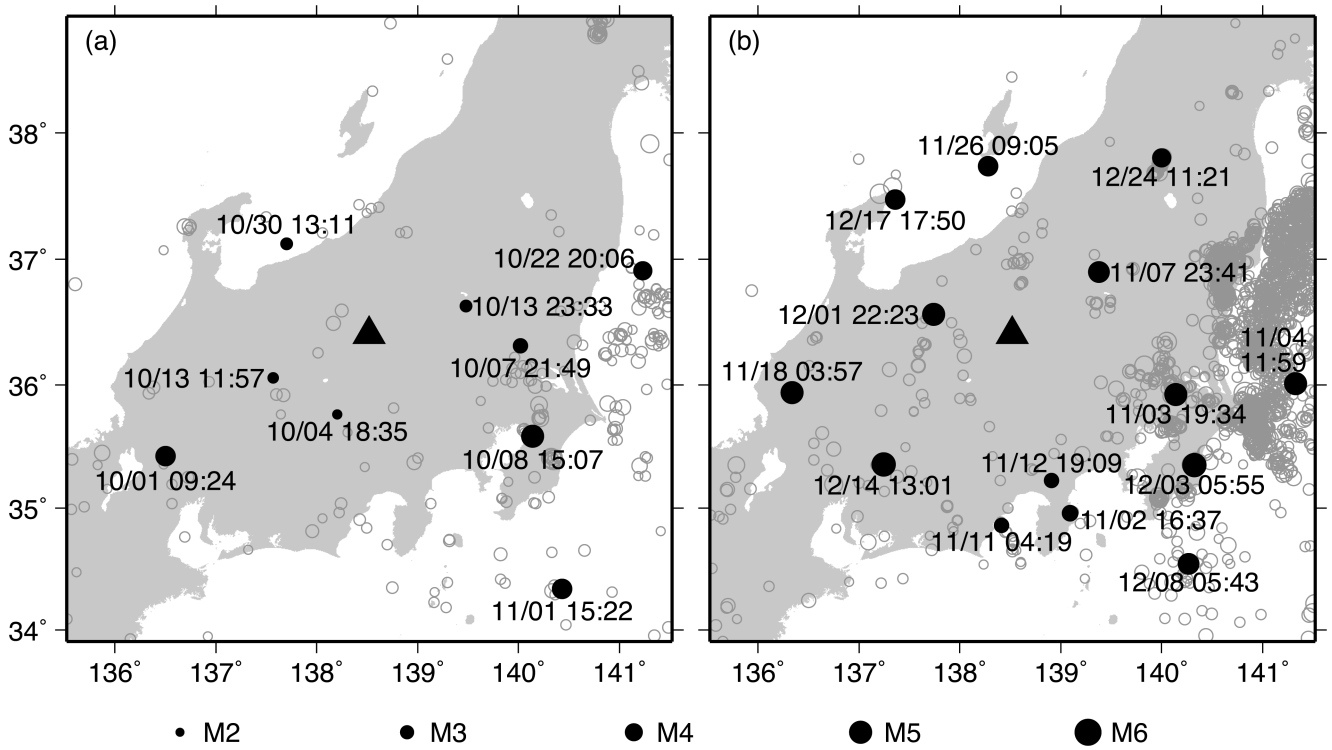

Figure 4. Earthquakes used for estimating site amplification factors in time periods (a) from 2008 September 30 to November 3 and (b) from 2011 November 1 to December 31 (black circles). Triangles indicate the location of Asama volcano. Grey circles show all the earthquakes in the catalogue issued by the Japan Meteorological Agency with magnitudes greater than 2 and depths less than 100 km occurred during individual analysis periods.

VLP events. Figs 2(b) and (c) show similar temporal variations, with almost no visible time lag between the amplitudes of the waveforms in the two frequency bands. To quantify the lag, we calculated cross-correlations between the waveforms in the VLP band and the envelope waveforms in the HF band for all events, creating a histogram representing the best-correlated time lags.

4 RESULTS

A spatial distribution of the residuals between observed and synthetic HF amplitudes for the main phase of a typical VLP event (Fig. 2) is given in Fig. 5(a). There is a region of small residuals at around 1500–2000 m above sea level beneath the crater. The best-fit location from the ASL analysis of the HF band (HF source; white stars) was south of and deeper than that identified by waveform inversion of the VLP band (VLP source; black stars). In Fig. 5(a), we also plot the spatial distribution of the residuals (black contours) between observed and synthetic waveforms in the VLP band, determined by waveform inversion in Maeda & Takeo (2011). The residual for the best-fit waveform was 23.1 per cent. There is a region of small residuals (of less than 30 per cent and indicated by the black contour closest to the VLP source) at above 1900 m above sea level in the northern region of the crater; this region in the VLP band was complementary to that in the HF band (see the N–S section, Fig. 5a), suggesting that the HF source was deeper than the VLP one.

To examine whether this depth difference was significant, we plotted the HF amplitudes for all stations against their distances from the two sources. The observed HF amplitudes were well fitted by eq. (1) against distance from the HF source (Fig. 5b; with a residual $E_{\rm best} = 14.2$ per cent), whereas the amplitudes were more scattered when plotted against the distance from the VLP source (Fig. 5c; with a residual $E_{\rm vlp} = 24.7$ per cent). Here the residuals were defined by

$$E_{\rm best} = [\Sigma_{n=1}^{N}\left(A_n^{\rm obs} - A_n^{\rm syn,best}\right)^2 / \Sigma_{n=1}^{N}\left(A_n^{\rm obs}\right)^2]^{1/2} \quad (3)$$

and

$$E_{\rm vlp} = [\Sigma_{n=1}^{N}\left(A_n^{\rm obs} - A_n^{\rm syn,vlp}\right)^2 / \Sigma_{n=1}^{N}\left(A_n^{\rm obs}\right)^2]^{1/2}, \quad (4)$$

where N is the number of stations, $A_n^{\rm obs}$ is the observed HF amplitude at nth station, and $A_n^{\rm syn,best}$ and $A_n^{\rm syn,vlp}$ are synthetic HF amplitudes at nth station calculated from the best-fit and VLP source locations, respectively. The significance of the residual difference between the two solutions is examined by the F-test. We assumed that $A_n^{\rm obs} - A_n^{\rm syn,best}$ and $A_n^{\rm obs} - A_n^{\rm syn,vlp}$ obey Gaussian distributions with average 0 and standard deviations $\sigma_{\rm best}$ and $\sigma_{\rm vlp}$, respectively. The ratio $\sigma_{\rm vlp}^2/\sigma_{\rm best}^2$ can be evaluated by $E_{\rm vlp}^2/E_{\rm best}^2$, which obeys the F-distribution with the freedom $(N-1, N-1)$. In the case of the analysed event, $N = 25$ and $E_{\rm vlp}^2/E_{\rm best}^2 = 24.7^2/14.2^2 = 3.03$ which exceeds 1 per cent point (2.66) of the F-distribution, indicating that the residual difference between 14.2 and 24.7 per cent is significant for 1 per cent significance level.

We also compared the amplitudes at stations on the crater rim (KA5, KA6, KA8, KA9, KAE and KAW) with those outside the rim in the summit region (KA0–KA3, KME and KMS). If the amplitudes at stations on the crater rim were systematically larger than those outside the rim, then a shallow source would be expected. In the VLP band, the spectral amplitudes at stations on the crater rim were systematically larger than those outside the rim (Fig. 2d). This distance-dependent amplitude distribution is unlikely explained by a radiation pattern given a semi-vertical tensile crack-like source mechanism (Maeda & Takeo 2011). It would more easily be explained by a shallow source. We found no such systematic amplitude difference in the HF band between the two station groups (Fig. 2d). Consistent with this observation, the observed HF amplitudes at the stations outside the rim were larger than synthetic ones, when plotted against distance from the VLP source (Fig. 5c). We note that, even though a radiation pattern might remain in the HF band when observed at very close distances, the large scatter in Fig. 5(c) is unlikely explained by it because the spatial distribution of the HF amplitudes does not show what is expected from the VLP source mechanism (approximately an N–S opening semi-vertical tensile crack; Maeda & Takeo 2011). These observations suggest that the HF source was indeed deeper than the VLP one.

We carried out ASL analyses for the main phase for all 1437 events in the 2008–2009 period and 571 events in the 2015 period. The number of events located at each grid node is shown in Fig. 6(a). Most events were located southwest and downward of the location of the VLP source (stars). The elevations of the HF source were 1997 (average) ± 71 (standard deviation) m for the 2008–2009 period and 1935 ± 116 m for the 2015 period. The larger standard deviation for the 2015 period may be related to the number of summit stations, which was smaller in 2015 than in 2008–2009. The HF source location of the eruptive VLP event (diamonds) was within the HF source region of normal VLP events. In Fig. 6(b), we show the average source amplitude of the events located at each grid node. Deeper events tended to have larger source amplitudes. The standard deviation for the source amplitude at each depth was relatively large because the frequency distribution of the source amplitude did not resemble a Gaussian distribution. As in the Gutenberg–Richter relationship for tectonic earthquakes, smaller events took place more frequently than larger events at each depth (Fig. 6c). The distributions at different depths show that large events were relatively more frequent at greater depth, resulting in the average source amplitude increasing with depth (Fig. 6b). This tendency was unlikely an artefact of the detection limit, given that our event selection criteria (Appendix A) required the signals to be observed at flank stations located lower than the source altitudes.

We investigated the effects of assumed Q values, velocity structures and error in the site amplification factors on the ASL results (Appendices B and D). In all cases, the HF sources were deeper than the VLP ones.

In Fig. 7(a), we compare the seismic moment M_0 from the VLP band and source amplitude S_0 of the main phase of the HF band for 18 VLP events having both estimates. A linear relationship, with S_0 (m^2 s^{-1}) $= 1.03 \times 10^{-15}$ M_0 (N m), was obtained from this analysis using the 60 s window (circles), with the coefficient of determination $R^2 = 0.928$. Using the 10 s moving window, a less clear relationship between S_0 and M_0 (triangles) was obtained ($R^2 = 0.867$). Given the 60 s window covered the entire duration of each event, while the 10 s window did not, the S_0 obtained from the 60 s window was regarded as representative of the cumulative amplitude of an event, while that from the 10 s window was more closely related to the maximum amplitude of the event. Thus, Fig. 7(a) suggests that the seismic moment correlated better with the cumulative amplitude than the maximum amplitude of the HF band. Figs 7(b) and (c) show a relationship between the vertical displacement amplitude at station KAE ($U_{\rm KAE}$) in the VLP band and the source amplitude of the HF band. A linear relationship, with $S_0 = aU_{\rm KAE}$, was observed, having best-fit slopes of $a = 2.07 \times 10^1$ m s^{-1} for the 2008–2009 period and $a = 1.63 \times 10^1$ m s^{-1} for the 2015 period. The displacement amplitude and source amplitude for the eruptive VLP event (Fig. 3)

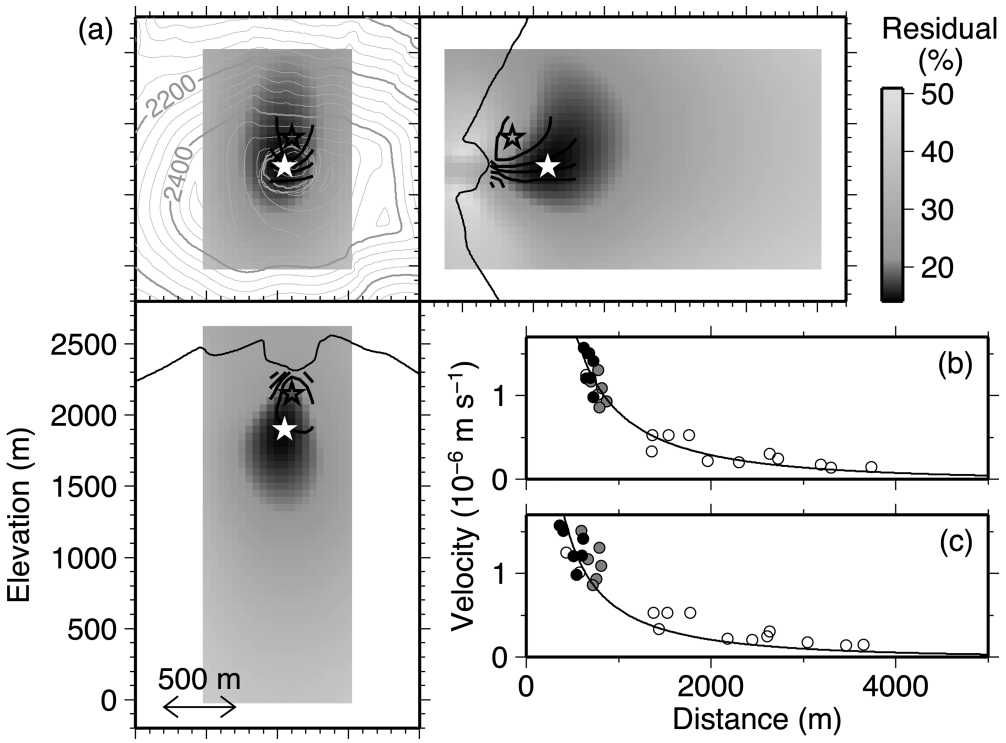

Figure 5. Results of the ASL analysis of the main phase of the VLP event shown in Fig. 2. (a) A spatial distribution of the residual between observed and synthetic HF amplitudes (grey scale); minimum values along the orthogonal directions are plotted on horizontal, E–W and N–S sections. White and black stars represent the best-fit locations from the ASL analysis of the HF band (HF source) and waveform inversion of the VLP band (VLP source; Maeda & Takeo 2011), respectively. Black contours represent the residuals (at 10 per cent intervals) between observed and synthetic waveforms of the VLP band from the waveform inversion of Maeda & Takeo (2011). Grey contours represent the topography. (b) Comparisons of observed (circles) and synthetic (lines) HF amplitudes plotted against their distances from the HF source and (c) from the VLP source, assuming the HF signals originated from the VLP event source location. Black- and grey-filled circles represent the data at stations on the crater rim (KA5, KA6, KA8, KA9, KAE and KAW) and outside the rim but within 1 km of the crater (KA0-KA3, KME and KMS), respectively. The amplitudes at other stations having intermediate or greater distances are plotted with open circles.

were larger than those of normal VLP events, with values near the fitting line for normal VLP events (Fig. 7c, diamond).

Figs 2(b) and (c) show similar temporal variations, with almost no visible time lag between the amplitudes of the waveforms in the VLP and HF bands. This suggests that the time lag, even if exists, is negligibly small compared to the timescale of the duration of each VLP event. Indeed, a histogram showing the best-correlated time lags between the waveform of the VLP band and the envelope waveform of the HF band (Figs 7d and e) showed that lags were 0.93 (average) ± 2.12 (standard deviation) s for the 2008–2009 period and 0.04 ± 2.19 s for the 2015 period. This suggests that the VLP signal occurred almost simultaneously (within one standard deviation) to the main phase of the HF signal.

The number of events at each grid node for the precursory phase analysis for the 2008–2009 period is shown in Fig. 8(a). Events were located at 1789 ± 196 m above sea level. Standard deviation of the elevations was relatively large, and the elevation where events were most frequently recorded (or the mode) was 1900 m above sea level (Fig. 8a). The average elevation for the precursory phase was less than that for the main phase. The elevation of the mode for the precursory phase was also less than that of the average for the main phase, although the difference between them was smaller than that between the averages of the two phases. The relationship between the source amplitudes of the precursory and main phases showed a positive correlation but with a relatively large scatter (Fig. 8b). In Fig. 8(c), we plot the number of VLP events with and without a precursory phase, showing that larger events were more frequently associated with a precursory phase of a detectable level.

5 DISCUSSION

Maeda & Takeo (2011) investigated the source time functions of six moment tensor components in the VLP band using waveform inversion. The moment tensor was consistent with an inflation/deflation source having an eigenvalue ratio of 5:3:2. There were several source geometries compatible with this eigenvalue ratio, including inflation of a tensile crack and a pipe (3:1:1 + 2:2:1 = 5:3:2; Maeda & Takeo 2011), two orthogonal tensile cracks (9:3:3 + 1:3:1 = 10:6:4) and fluid movement from a sphere to a thin ellipsoidal crack with pressure recovery (Mizuno *et al.* 2015). All these candidate geometries involve a semi-vertical tensile crack. Estimates based on the largest principal axis show that the crack opens approximately in an N–S direction (Maeda & Takeo 2011). The source time functions of the moment tensors show an initial rapid inflation of the source volume on a timescale of 10 s, followed by a gradual deflation on a timescale of 100 s (Maeda & Takeo 2011). Several tens of seconds after each VLP event, an episodic degassing event occurs from a vent at the crater floor, with the amount of degassing being proportional to the seismic moment of the VLP event (Kazahaya *et al.* 2011). This suggests that deflation is related to gas escaping from the VLP source to the surface. In contrast, inflation is assumed to be caused by an

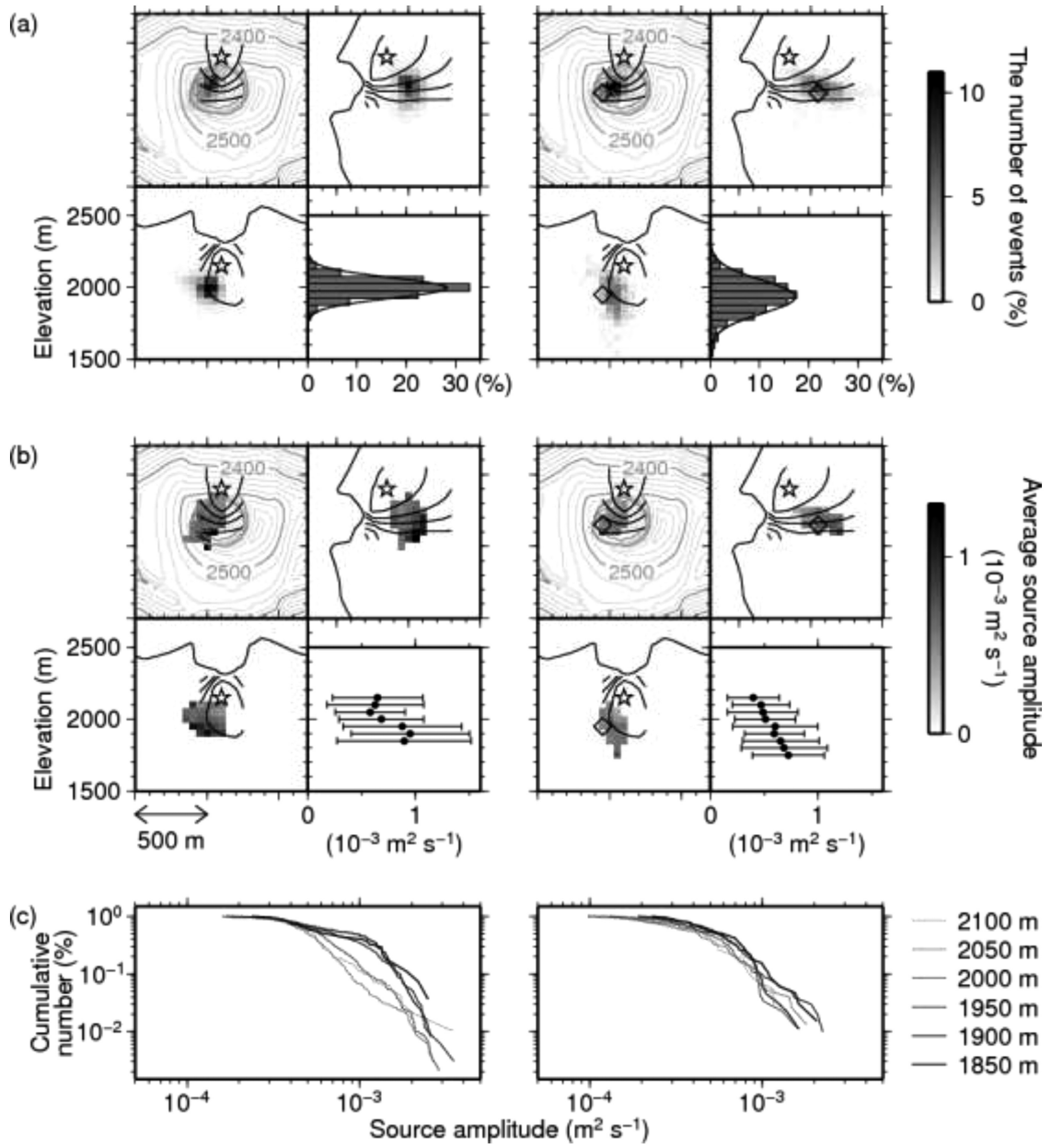

Figure 6. Results of the ASL analysis of the main phase of all VLP events. (a) The numbers of events located at each grid node for the 2008–2009 (left) and 2015 (right) analysis periods. (b) Average source amplitudes at each grid node for these periods, plotted for grid nodes having more than 10 events. The top left, bottom left and top right frames in each panel show horizontal, E–W and N–S sections, respectively. The quantities are summed/averaged over the orthogonal axes. The bottom right frame in each panel shows the quantities summed/averaged over the horizontal plane at each elevation; the curves in panel (a) and the bars in panel (b) represent Gaussian fits and standard deviations, respectively. Stars and black contours indicate the best-fit VLP source location and the spatial distribution of the residual between observed and synthetic waveforms in the VLP band (at 10 per cent intervals) from the waveform inversion of Maeda & Takeo (2011). Diamonds represent the HF source location for the eruptive VLP event shown in Fig. 3. Grey contours represent the topography. (c) Histograms for the source amplitude versus the cumulative number of events at each elevation for the two analysis periods.

inflow of gas from greater depth to the VLP source (Kazahaya *et al.* 2015). In summary, the VLP events at Asama volcano are related to a rapid inflow of volcanic gas from depth into an N–S-opening semi-vertical crack-like source volume on the timescale of 10 s, followed by a gradual escape of the gas from the source volume to the surface over a timescale of 100 s.

The HF oscillation associated with VLP events lasts for 10–20 s. The first arrival of this signal is unclear (Fig. 2c). These characteristics are consistent with volcanic tremors. One of the most common interpretations of the process underlying volcanic tremors is a flow-induced oscillation within a narrow passage (e.g. Julian 1994). In our VLP source model for Asama volcano, fluid flows may exist below and above the VLP source, corresponding to inflow and outflow of gas, respectively. Our ASL analysis indicates that the HF source of the main phase is deeper than the VLP source, suggesting that the HF oscillation is caused by inflow of gas from a depth greater than that of the VLP source. The longer duration of the gas outflow from the VLP source to the surface produces seismic signals that are weaker than those associated with rapid gas inflows to the VLP source.

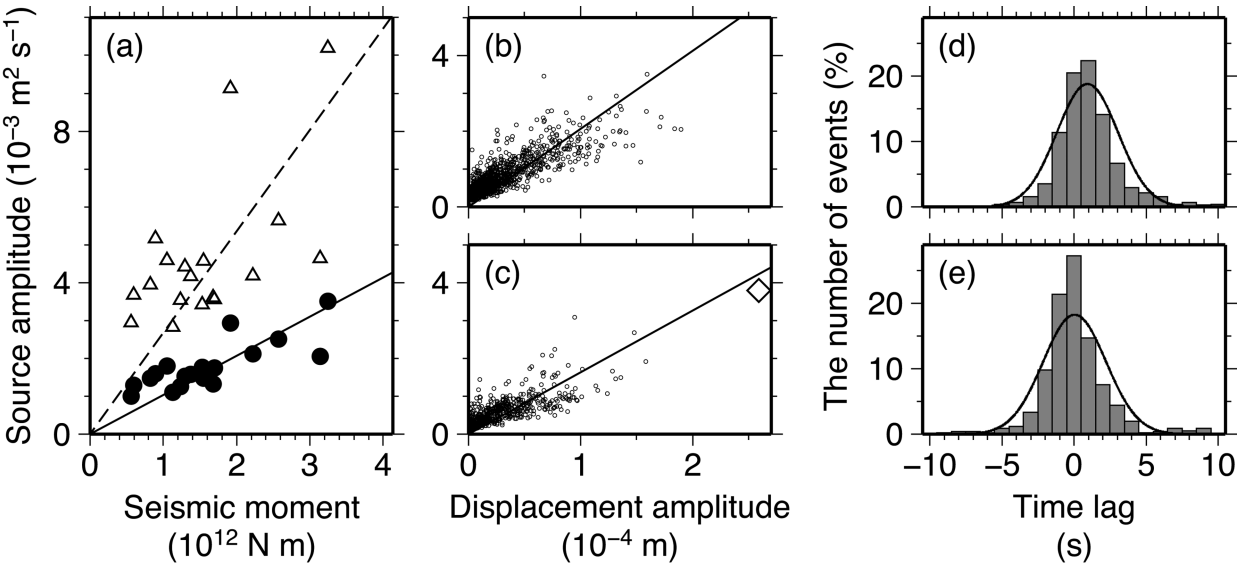

Figure 7. Comparison of event sizes and timings derived from the VLP and HF bands. (a) A relationship between the seismic moment in the VLP band and the source amplitude in the HF band for the 18 events in 2008 that have both estimates (circles and the solid line: 60 s window; triangles and dashed line: 10 s window). (b) Relationship between the vertical displacement amplitude at station KAE in the VLP band and the source amplitude in the HF band (60 s window) for the 2008–2009 and (c) 2015 analysis periods. The diamond shows the relationship for the eruptive VLP event shown in Fig. 3. The horizontal axis scales for seismic moment (panel a) and displacement amplitude (panels b and c) were chosen to be consistent with eq. (2). (d) The best-correlated time lags between the waveform of the VLP band and the envelope of the HF band from the vertical component at KAE for the 2008–2009 and (e) 2015 analysis periods. A positive sign indicates that the HF oscillation occurred later than the VLP signal. The lines represent Gaussian fits to the data.

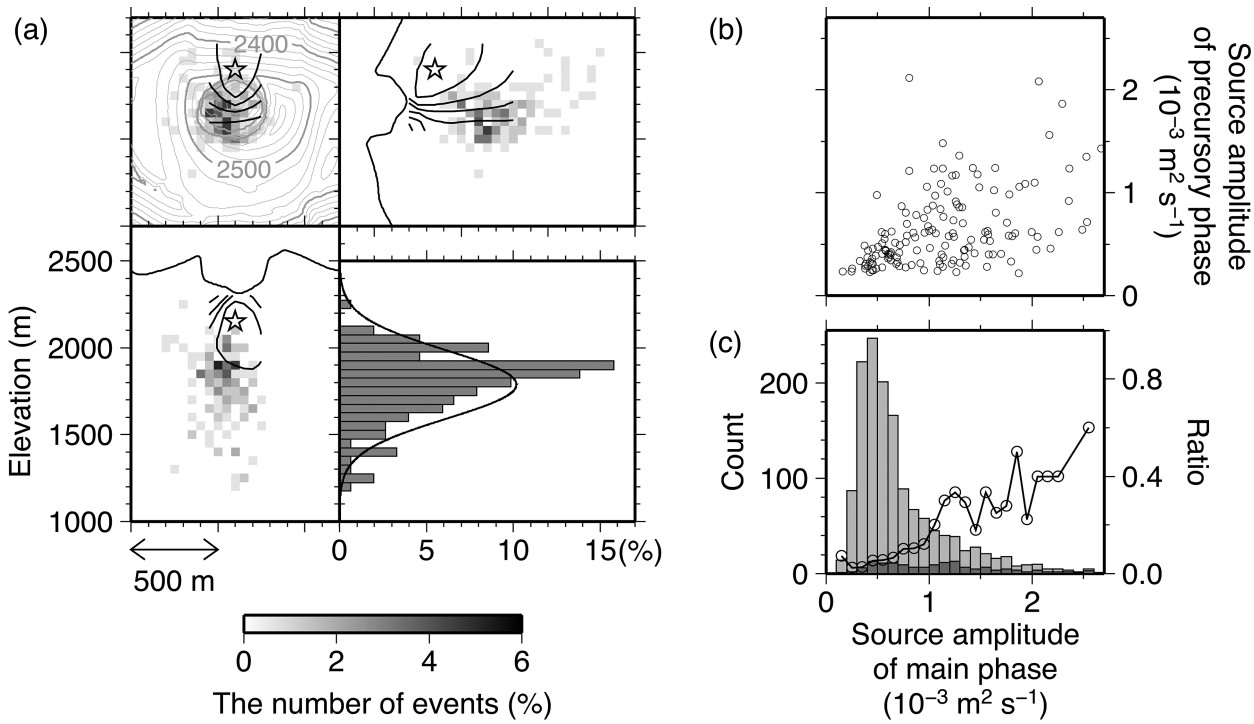

Figure 8. Results of the ASL analysis of the precursory phase. (a) The number of events located at each grid node for the 2008–2009 analysis period. (b) The relationship between the source amplitudes of the main and precursory phases. (c) The numbers of events with and without a detectable precursory phase in each source amplitude range (dark and light grey bars, respectively). The line with the circles represents the ratio of the number of events having a precursory phase.

The occurrence of the HF signal at a deeper location than the VLP one is opposite to analysis results for a seismic swarm at White Island in New Zealand (Jolly *et al.* 2017). The model of Ohminato (2006) for VLP events at Satsuma-Iwojima volcano in Japan also assumed that HF oscillations occur at an outlet side of the VLP source. In the case of White Island, the VLP signal starts earlier than the HF one, and the durations in the two bands are different with each other (fig. 4c in Jolly *et al.* 2017). In the

case of Satsuma-Iwojima, the HF oscillations start after the occurrence of each VLP event (fig. 4 in Ohminato 2006). In contrast, the HF signal at Asama volcano is almost synchronized with the VLP one (Figs 2 and 7), suggesting that the excitation mechanisms of the HF oscillations at the three volcanoes are different with each other.

The depth difference between the VLP and HF sources at Asama volcano was estimated to be ∼150 m (Figs 5 and 6a). Despite this spatial separation, almost no time lag was found between the signals of these two bands (Figs 7d and e). In addition, temporal variation of the HF amplitude was consistent with the waveform of the VLP band (Figs 2b and c), while the source amplitude of the HF band correlated well with the seismic moment of the VLP band (Figs 7a–c). These observations suggest a strong connection between the two sources, in which the VLP source immediately and directly responds to the HF source. This immediate response is not an instantaneous phenomenon but continues over a 10–20 s interval for each VLP event, suggesting a relatively stable connection.

Taking into account these constraints, we proposed a conceptual model (Fig. 9a) for the VLP and associated HF signals. In this model, gas exsolved from the magma travels upwards, through the semi-vertical crack-like cavity (imaged using waveform inversion), until it reaches a permeability boundary, at which point further ascent is blocked. The HF and VLP signals are generated by the upward gas flow into the cavity and resultant inflation at the cavity, respectively. To understand this model, note that both the waveform inversion and ASL analysis use point source approximations, whereas the real source has a finite size. It is likely that the signals of both bands are emitted from the entire cavity but with different spatial intensity distributions. The gas accumulation and resultant inflation, observed as the VLP signal, mainly occur near the roof of the cavity, because the low-density gas phase will migrate upward under buoyancy. The HF oscillation appears to be emitted more intensely from near the lowest end of the cavity, where the aperture is expected to be narrower than that near the roof (Fig. 9a); the gas flow through a narrow passage has been considered a candidate source process of tremor-like signals (e.g. Julian 1994; Ohminato 2006). This spatial difference results in different point source locations for the two bands, although the rapid equilibration of the gas pressure within the cavity (at the sound speed of the gas; several hundred meters per second assuming a single gas phase in the cavity) yields almost no time lag and similar temporal variations in both frequency bands. Note that the depth difference of ∼150 m is too large to let gas move between them instantly; a time lag of more than several tens of seconds between each VLP event and the following eruption/degassing event suggests a gentle gas flow at velocities substantially less than the sound speed. A similar discussion has been made by Jolly *et al.* (2018) to distinguish a mass movement and a stress perturbation.

We examined this conceptual model by evaluating the observed and expected source depth differences between the two bands for the typical VLP event occurring at 17:18:13 on 2008 October 28 (Fig. 2). Maeda & Takeo (2011) determined the principal moment tensor of this event to be (5.598, 3.387, 2.260) × 10^{12} N m, which they interpreted as simultaneous inflations of a tensile crack and a pipe. The inflation within the tensile crack by volume ΔV results in a moment tensor of ($3\mu\Delta V$, $\mu\Delta V$, $\mu\Delta V$), while that in the pipe gives ($2\mu\Delta V$, $2\mu\Delta V$, $\mu\Delta V$), yielding a total of ($5\mu\Delta V$, $3\mu\Delta V$, $2\mu\Delta V$) assuming a common ΔV for the crack and pipe, where μ is the rigidity of the surrounding elastic medium. Comparing this theoretical expression for the principal moment tensor with observed values, using $\mu = 4.3 \times 10^9$ Pa (Maeda & Takeo 2011), we obtain $\Delta V = \{[5.598/(5\mu) + 3.387/(3\mu) + 2.260/(2\mu)]/3\} \times 10^{12}$ N m $= 2.6 \times 10^2$ m^3. This volume change for the tensile crack can be explained by a 0.01 m opening of a 260 m × 100 m crack, although the opening dislocation and area of the crack cannot be uniquely determined from the volume change. This calculation suggests that assuming a tensile crack source, the observed depth difference of 250 m between the VLP and HF sources for this event (Fig. 5) would represent the height of the crack.

In this model, the temporal variation of the source cavity volume $V(t)$ is controlled by the inflow and outflow of the gas given by the relationship:

$$\mathrm{d}V(t)/\mathrm{d}t = Q_{\mathrm{in}}(t) - Q_{\mathrm{out}}(t), \tag{5}$$

where t is time, and $Q_{\mathrm{in}}(t)$ and $Q_{\mathrm{out}}(t)$ are volume fluxes of the inflow and outflow, respectively. We neglected temporal variation of the gas pressure, because it is expected to equalize with lithostatic pressure through cavity wall deformation over a short time frame. As was mentioned earlier, the timescale of the outflow (∼100 s) is an order of magnitude larger than that of the inflow (∼10 s), suggesting that the relationship $Q_{\mathrm{in}}(t) \gg Q_{\mathrm{out}}(t)$ holds during the initial stage of each event. During this initial period, eq. (5) can be simplified to

$$\mathrm{d}V(t)/\mathrm{d}t = Q_{\mathrm{in}}(t), \tag{6}$$

showing inflation directly related to the inflow. We focused on this inflation stage, during which strong HF signals were observed (Fig. 2c). The left-hand side of eq. (6) is proportional to the moment rate function, which is in turn proportional to the seismic velocity in the near field, when traveltime from the source is substantially smaller than the timescale of the source time function (e.g. Aki & Richards 2002). In this case, we have

$$v_{\mathrm{VLP}}(t) \propto \mathrm{d}M(t)/\mathrm{d}t \propto \mathrm{d}V(t)/\mathrm{d}t = Q_{\mathrm{in}}(t), \tag{7}$$

where $v_{\mathrm{VLP}}(t)$ and $M(t)$ are the near-field seismic velocity and the moment function, respectively. Typically, the near-field term is dominant in the VLP band, because its form approximates time integration of the far-field terms; the time integration is equivalent to a division by angular frequency in the frequency domain, which amplifies the low-frequency content. Thus eq. (7) suggests that the typical duration of 10–20 s of each VLP event is characteristic of the gas inflow interval.

A quantitative relationship between the volume flux $Q_{\mathrm{in}}(t)$ and the HF amplitude $|v_{\mathrm{HF}}(t)|$ may be complex, but it is natural to assume that a larger volume flux $Q_{\mathrm{in}}(t)$ produces a larger amplitude HF signal, assuming that the VLP events start by episodic inflow of the gas. In the simplest case, we assumed the relationship: $Q_{\mathrm{in}}(t) \propto |v_{\mathrm{HF}}(t)|$. In this case, eq. (7) reduces to

$$v_{\mathrm{VLP}}(t) \propto \mathrm{d}M(t)/\mathrm{d}t \propto |v_{\mathrm{HF}}(t)|, \tag{8}$$

which is consistent with our observation that the VLP waveform and HF amplitude have similar temporal variations (Fig. 2). Integrating eq. (8) with time gives

$$M_0 = M(t_{\mathrm{e}}) - M(t_{\mathrm{s}}) \propto \int_{t_{\mathrm{s}}}^{t_{\mathrm{e}}} |v_{\mathrm{HF}}(t)|\,\mathrm{d}t, \tag{9}$$

where t_{s} and t_{e} are the start and end times of the gas inflow. Because our analysis time window of 60 s encompasses the period from t_{s} to t_{e}, the right-hand side of eq. (9) should be positively correlated with the source amplitude of the HF signal. Thus, eq. (9) underlies the linear relationship between seismic moment and source amplitude (Fig. 7a).

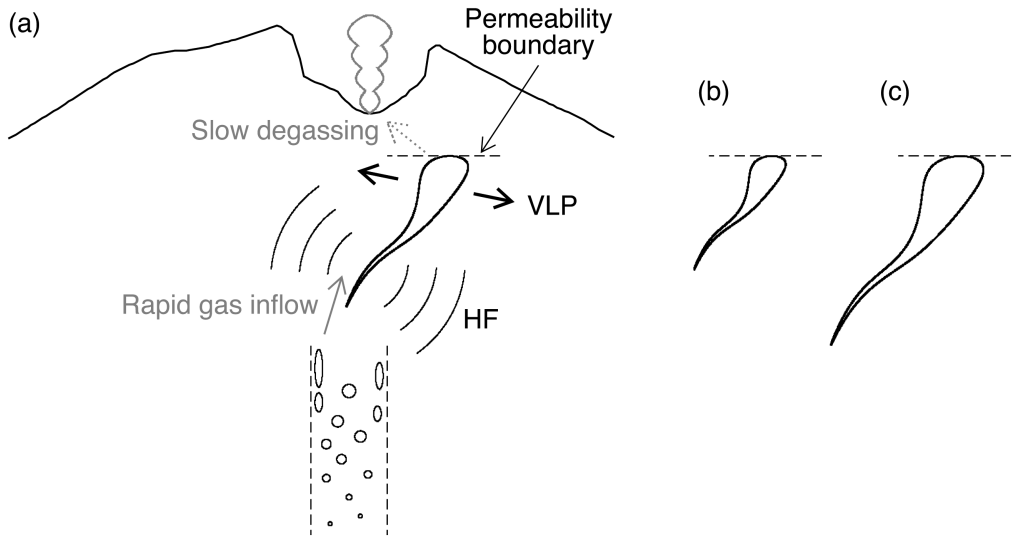

Figure 9. (a) Schematic illustration of the VLP and HF source processes. Schematic images of the source cavities for (b) small and (c) large events, showing that the location of the bottom of the crack is more sensitive than that of the centroid of the crack to event size.

The assumption that $Q_{\rm in}(t) \propto |v_{\rm HF}(t)|$ may be difficult to validate using models having flow-induced oscillation along a single pathway, but the validation may be realized using models having simultaneous flow-induced oscillations from many small channels. In this case, the oscillation amplitude $|v_{\rm HF}(t)|$ may be proportional to the number of gas flow channels, which may in turn be proportional to the net volume flux $Q_{\rm in}(t)$. A similar scenario was discussed in Battaglia *et al.* (2005). This interpretation is also consistent with an isotropic radiation pattern. Previous ASL studies have assumed multiple scattering of an *S* wave to produce isotropic radiation (Kumagai *et al.* 2010). However, our analysis is based on data collected at stations that were, in some cases, only several hundred metres from the source. At such close distances, the wave may be insufficiently scattered to achieve isotropic radiation as the mean free path for Asama volcano has been estimated to be up to 1 km (Yamamoto & Sato 2010). A numerical simulation of scattering (Kumagai *et al.* 2011b) also suggests that a distance of several hundred metres is insufficient to achieve isotropic *S*-wave radiation. In Appendix C, we show that eq. (1) is better than the theoretical distance–amplitude relationship of eq. (C1) in explaining the data, although the latter is expected to hold under conditions of multiple scattering (Fig. C1). These data suggest that multiple scattering is not dominant in our case; nevertheless, the observed amplitudes were explained well by isotropic radiation (Fig. 5b). We surmise that isotropic radiation in the HF band of the VLP events at Asama volcano is realized via simultaneous oscillation of many subvertical channels whose azimuths are randomly oriented. Thus, the radiation pattern at the source is already isotropic, and the ASL analysis based on eq. (1) works without notable scattering. Similar interpretation has been proposed by Taisne *et al.* (2011).

Larger events tend to have HF sources at greater depth (Figs 6b and c). As was mentioned earlier, this tendency is unlikely an artefact of the detection limit since we used only the events observed at flank stations located lower than the source altitudes. Rather, this observation is explained as follows: because larger events have a greater gas-filled cavity, its bottom is deeper, even though the centroid of the inflation (VLP source) appears to be only weakly related to event size (Figs 9b and c).

Some VLP events were associated with a precursory phase, exemplified by the small oscillation portion occurring at 17:17:50–17:18:10 in Fig. 2(c). Among the 1437 events analysed for the 2008–2009 period, at least 152 events had a detectable precursory phase, satisfying our detection criteria that required the signal-to-noise ratio to exceed 2. We observed that larger events were more frequently associated with a detectable precursory phase (Fig. 8c), suggesting that some seismic events without the detected precursory phase were associated with precursory phases having signal-to-noise ratios that were below the detection threshold. The source location of the precursory phase was deeper than that of the main phase, implying that the precursory phase may be related to gas exsolution or gas flow at a region deeper than the VLP event source cavity. The relatively large time difference of ∼20 s between the precursory and main phases (Fig. 2c) as well as the relatively large scatter among their source amplitudes (Fig. 8b) indicate that some spatial separation may exist between sources of precursory and main phase signal components.

The eruptive VLP event (Fig. 3) had a larger displacement amplitude and source amplitude than other VLP events (Fig. 7). Except for this difference, our results for eruptive versus normal VLP events were similar (Figs 6 and 7), suggesting that an eruptive VLP event takes place essentially via the same process as other VLP events, but with larger gas inflows that last longer (Fig. 3). The accumulation of large amounts of gas in the cavity provides sufficient energy for an eruption to occur. We note that VLP events with exceptionally long durations also occurred immediately before the three small eruptions in 2008. Thus, the amount of gas that flows into the cavity during a VLP event may be the controlling factor behind eruptions.

6 CONCLUSIONS

In this study, we conducted an ASL analysis of the HF (5–10 Hz) oscillation associated with VLP seismic events at Asama volcano in Japan. We analysed 1437 events from a dense field campaign in 2008–2009, as well as 571 events surrounding an eruptive period in 2015, including a VLP event that immediately preceded an eruption. The locations of the HF source of the main phase were deeper

for larger events. They were, on average, ∼150 m deeper than the VLP band source region identified in our previous waveform inversion study (Maeda & Takeo 2011). Despite this depth difference, the cross-correlations between the envelope waveforms of the HF band and the waveforms of the VLP band showed almost no time lags. The source amplitude, a measure of the event size from ASL analysis of the HF band, correlated well with both seismic moment and displacement amplitude, which are measures of the event size derived from the VLP band. Some events were preceded by ∼20 s by another small oscillation in the HF band, identified as a precursory phase. The ASLs of the precursory phase were, on average, ∼200 m deeper than those of the main phase. The source amplitude of the precursory phase showed a positive correlation with that of the main phase, although this relationship was weak. The results for both normal and eruptive VLP events were similar, except that the eruptive VLP event was larger in size.

We surmise that the HF (main phase) and VLP signals were caused by an inflow of volcanic gas from depth into an N–S-opening semi-vertical crack-like cavity (imaged in our previous waveform inversion study) and a resultant inflation of the cavity, respectively. The gas accumulation and resultant inflation, observed as the VLP signal, were centred within the upper region of the cavity, whereas the HF oscillation was emitted more intensely from lower and narrower parts of the cavity. This explains the depth difference of ∼150 m between the two sources. Because they are related to different parts of the same gas-filled volume, the VLP and HF band sources immediately and directly respond to each other, resulting in similar temporal variations with almost no time lag and well-correlated amplitudes between the signals of these two bands. The eruptive VLP event was likely to be caused by the same process but involved a greater gas inflow of longer duration. This larger amount of gas provided sufficient energy for an eruption to take place. Thus, the volume of the gas inflow appears to underpin eruptions at this site.

ACKNOWLEDGEMENTS

Discussions with Atsuko Namiki improved the interpretation of our analyses. Hiroyuki Kumagai highlighted several points to be addressed in the evaluation of the robustness of the results. Takeshi Nishimura suggested using the theoretical expression for the HF amplitudes. Comments by two anonymous reviewers helped to improve the manuscript. This study was supported by the Joint Usage/Research Center program of Earthquake Research Institute, the University of Tokyo. We thank Dr Trudi Semeniuk and Tina Tin from Edanz Group (www.edanzediting.com/ac) for editing a draft of this manuscript.

Author contribution statement: YM collected the 2008–2009 campaign data, conducted the ASL analyses and drafted the manuscript. MT collected the data during both the 2008–2009 and 2015 periods at campaign and permanent seismic stations. RK performed the detection of the VLP events. All authors discussed the source process of the analysed events and checked the manuscript.

REFERENCES

Aki, K. & Chouet, B., 1975. Origin of coda waves: source, attenuation, and scattering effects, *J. geophys. Res.,* **80**(23), 3322–3342.

Aki, K. & Richards, P., 2002. *Quantitative Seismology,* 2nd edn, University Science Books.

Aoki, Y. *et al.*, 2009. *P*-wave velocity structure beneath Asama Volcano, Japan, inferred from active source seismic experiment, *J. Volc. Geotherm. Res.,* **187**(3-4), 272–277.

Battaglia, J. & Aki, K., 2003. Location of seismic events and eruptive fissures on the Piton de la Fournaise volcano using seismic amplitudes, *J. geophys. Res.,* **108**(B8), 2364.

Battaglia, J., Aki, K. & Staudacher, T., 2005. Location of tremor sources and estimation of lava output using tremor source amplitude on the Piton de la Fournaise volcano: 2. Estimation of lava output, *J. Volc. Geotherm. Res.,* **147**(3-4), 291–308.

Caudron, C. *et al.*, 2018. Seismic amplitude ratio analysis of the 2014–2015 Bárðarbunga-Holuhraun dike propagation and eruption, *J. geophys. Res.,* **123**(1), 264–276.

Chouet, B. *et al.*, 2003. Source mechanisms of explosions at Stromboli Volcano, Italy, determined from moment-tensor inversions of very-long-period data, *J. geophys. Res.,* **108**(B1), 2019.

Chouet, B., Dawson, P. & Arciniega-Ceballos, A., 2005. Source mechanism of Vulcanian degassing at Popocatepetl Volcano, Mexico, determined from waveform inversions of very long period signals, *J. geophys. Res.,* **110**(B7), B07301.

Chouet, B.A. & Matoza, R.S., 2013. A multi-decadal view of seismic methods for detecting precursors of magma movement and eruption, *J. Volc. Geotherm. Res.,* **252,** 108–175.

Hidayat, D., Chouet, B., Voight, B., Dawson, P. & Ratdomopurbo, A., 2002. Source mechanism of very-long-period signals accompanying dome growth activity at Merapi volcano, Indonesia, *Geophys. Res. Lett.,* **29**(23), 2118.

James, M.R., Lane, S.J. & Chouet, B.A., 2006. Gas slug ascent through changes in conduit diameter: Laboratory insights into a volcano-seismic source process in low-viscosity magmas, *J. geophys. Res.,* **111**(B5), B05201.

Japan Meteorological Agency, 2015. 'Monthly Volcanic Activity Report (June 2015)'. Available at: http://www.data.jma.go.jp/svd/vois/data/tokyo/eng/volcano_activity/2015/2015_06_monthly.pdf. (accessed 4 June 2018).

Jolly, A., Lokmer, I., Christenson, B. & Thun, J., 2018. Relating gas ascent to eruption triggering for the April 27, 2016, White Island (Whakaari), New Zealand eruption sequence, *Earth Planets Space,* **70**(1), 177.

Jolly, A.D., Lokmer, I., Thun, J., Salichon, J., Fry, B. & Chardot, L., 2017. Insights into fluid transport mechanisms at White Island from analysis of coupled very long-period (VLP), long-period (LP) and high-frequency (HF) earthquakes, *J. Volc. Geotherm. Res.,* **343**(1), 75–94.

Julian, B.R., 1994. Volcanic tremor: Nonlinear excitation by fluid flow, *J. geophys. Res.,* **99**(B6), 11 859–11 877.

Kazahaya, R., Mori, T., Takeo, M., Ohminato, T., Urabe, T. & Maeda, Y., 2011. Relation between single very-long-period pulses and volcanic gas emissions at Mt. Asama, Japan, *Geophys. Res. Lett.,* **38**(11), L11307.

Kazahaya, R., Maeda, Y., Mori, T., Shinohara, H. & Takeo, M., 2015. Changes to the volcanic outgassing mechanism and very-long-period seismicity from 2007 to 2011 at Mt. Asama, Japan, *Earth planet. Sci. Lett.,* **418,** 1–10.

Kumagai, H. *et al.*, 2010. Broadband seismic monitoring of active volcanoes using deterministic and stochastic approaches. *J. geophys. Res.,* **115**(B8), B08303.

Kumagai, H., Placios, P., Ruiz, M., Yepes, H. & Kozono, T., 2011a. Ascending seismic source during an explosive eruption at Tungurahua volcano, Ecuador, *Geophys. Res. Lett.,* **38**(1), L01306.

Kumagai, H., Saito, T., O'Brien, G. & Yamashina, T., 2011b. Characterization of scattered seismic wavefields simulated in heterogeneous media with topography, *J. geophys. Res.,* **116**(B3), B03308.

Kumagai, H. *et al.*, 2013. Source amplitudes of volcano-seismic signals determined by the amplitude source location method as a quantitative measure of event size, *J. Volc. Geotherm. Res.,* **257,** 57–71.

Kurokawa, A., Takeo, M. & Kurita, K., 2016. Two types of volcanic tremor changed with eruption style during 1986 Izu-Oshima eruption, *J. geophys. Res.,* **121**(4), 2727–2736.

Maeda, Y. & Takeo, M., 2011. Very-long-period pulses at Asama volcano, central Japan, inferred from dense seismic observations, *Geophys. J. Int.,* **185**(1), 265–282.

Mizuno, N., Ichihara, M. & Kame, N., 2015. Moment tensors associated with the expansion and movement of fluid in ellipsoidal cavities, *J. geophys. Res.,* **120**(9), 6058–6070.

Morioka, H., Kumagai, H. & Maeda, T., 2017. Theoretical basis of the amplitude source location method for volcano-seismic signals, *J. geophys. Res.,* **122**(8), 6538–6551.

Nakamichi, H., Kumagai, H., Nakano, M., Okubo, M., Kimata, F., Ito, Y. & Obara, K., 2009. Source mechanism of a very-long-period event at Mt Ontake, central Japan: Response of a hydrothermal system to magma intrusion beneath the summit, *J. Volc. Geotherm. Res.,* **187**(3-4), 167–177.

Ogiso, M. & Yomogida, K., 2015. Estimation of locations and migration of debris flows on Izu-Oshima Island, Japan, on 16 October 2013 by the distribution of high frequency seismic amplitudes, *J. Volc. Geotherm. Res.,* **298** 15–26.

Ogiso, M., Matsubayashi, H. & Yamamoto, T., 2015. Descent of tremor source locations before the 2014 phreatic eruption of Ontake volcano, Japan, *Earth Planets Space,* **67,** 206.

Ohminato, T., 2006. Characteristics and source modeling of broadband seismic signals associated with the hydrothermal system at Satsuma-Iwojima volcano, Japan, *J. Volc. Geotherm. Res.,* **158**(3–4), 467–490.

Ohminato, T., Chouet, B.A., Dawson, P. & Kedar, S., 1998. Waveform inversion of very long period impulsive signals associated with magmatic injection beneath Kilauea volcano, Hawaii, *J. geophys. Res.,* **103**(B10), 23839–23862.

Ohminato, T., Takeo, M., Ichihara, M., Tsuji, H. & Watanabe, A., 2015. Small eruption at Mt. Asama on June 16, 2015, revealed from near field observations, *Abst. Volc. Soc. Jpn. Fall Meeting,* A3–A11, doi:10.18940/vsj.2015.0_39 (in Japanese).

Rautian, T.G. & Khalturin, V.I., 1978. The use of the coda for determination of the earthquake source spectrum, *Bull. seism. Soc. Am.,* **68**(4), 923–948.

Sparks, R.S.J., 2003. Dynamics of magma degassing, *Geol. Soc. London Spec. Publ.,* **213,** 5–22.

Taisne, B., Brenguier, F., Shapiro, N.M. & Ferrazzini, V., 2011. Imaging the dynamics of magma propagation using radiated seismic intensity, *Geophys. Res. Lett.,* **38**(4), L04304.

Takemura, S., Furumura, T. & Saito, T., 2009. Distortion of the apparent S-wave radiation pattern in the high-frequency wavefield: Tottori-Ken Seibu, Japan, earthquake of 2000, *Geophys. J. Int.,* **178**(2), 950–961.

Takeo, M., Maeda, Y., Kazahaya, R. & Aoki, Y., 2015. A relation between eruption and VLP activities from 2004 to 2015 at Asama volcano, *Abst. Volc. Soc. Jpn. Fall Meeting,* A3–A10, doi:10.18940/vsj.2015.0_38 (in Japanese).

Yamamoto, M. & Sato, H., 2010. Multiple scattering and mode conversion revealed by an active seismic experiment at Asama volcano, Japan, *J. geophys. Res.,* **115**(B7), B07304.

Yamamoto, M. *et al.*, 2005. A unique earthquake activity preceding the eruption at Asama volcano in 2004, *Bull. Volc. Soc. Jpn.,* **50**(5), 393–400.

Walsh, B., Jolly, A.D. & Procter, J., 2017. Calibrating the amplitude source location (ASL) method by using active seismic sources: an example from Te Maari volcano, Tongariro National Park, New Zealand, *Geophys. Res. Lett.,* **44**(8), 3591–3599.

APPENDIX A: DATA QUALITY CRITERIA USED FOR EVENT SELECTION

We detected VLP events by applying the algorithm of Kazahaya *et al.* (2015) to the vertical waveform of VLP signals recorded at station KAE (Fig. 1). This algorithm uses the signal-to-noise ratios in several frequency bands and the positive–negative pattern of the waveform to distinguish VLP events from tectonic earthquakes, microseismic noise and electronic noise. The time point having maximum amplitude in the 0.005–0.2 Hz band is referred to as the event time.

Some of the detected VLP events were not appropriate for the ASL analysis because of their small signal-to-noise ratios at distant stations or contamination from another earthquake signal. To evaluate data quality, we calculated the average envelope amplitude in a 5–10 Hz band in every 10 s window from 60 s before to 60 s after the event time derived from the waveform of event signals recorded at each station. In our analysis of the main phase, the waveform was considered good, if the envelope amplitude was maximal in the 10 s window immediately before or immediately after the event time (indicating no or little contamination from another event signal); this maximum amplitude needed to be more than twice the amplitude recorded 30–40 s before the event time (indicating a high signal-to-noise ratio). In our analysis of the precursory phase, the waveform was considered good, if the envelope amplitude in either the 10–20 or 20–30 s windows before the event time were more than twice that at 30–40 s before the event time (indicating the existence of a precursory phase with a large signal-to-noise ratio). In addition, the two criteria for the main phase must be satisfied. For the 2008–2009 period, we carried out ASL analysis of a given event, whenever the waveforms at 7 or more of the total 14 summit stations (located less than 1 km from the crater centre) and 6 or more of the total 12 flank stations (located 1–5 km from the crater centre) had good quality waveforms. In the 2015 period, we carried out the analysis when the waveforms at all permanent summit stations (KAE, KAW, KME and KMS), the northern station KMN and 6 or more flank stations had good form.

APPENDIX B: ASL ANALYSIS WITH DIFFERENT Q VALUES AND VELOCITY STRUCTURES

We carried out ASL analyses using Q values ranging from 20 to 100 (at intervals of 10). We also used a value of $Q = 110$ to discriminate between events having a best Q of 100 from those with a larger best Q. We evaluated the suitability of the Q value using two criteria. One was the residual between the observed and synthetic HF amplitudes averaged over all events, yielding $Q = 50$ as the best value (Fig. B1a). We calculated the square root of the average of the square residuals for all events (instead of using a simple average of the residuals) to ensure consistency with maximizing the total probability density for a Gaussian distribution. The second criterion was to tally the number of events for which the residual was minimal at each Q value. Using this criterion, $Q = 40$ had the best result, with $Q = 50$ being the second-best option (Fig. B1b). Figs B1(a) and (b) suggest that $Q = 50$ is a plausible assumption. Fig. B1(c) shows spatial distributions of the numbers of events located at each grid node for Q values ranging from 20 to 100. Compared with $Q = 50$ (Fig. 6a), $Q = 20$ and $Q = 100$ resulted in deeper and shallower source locations, respectively. Even in the case of $Q = 100$, the source locations for most events were located outside of the small residual region of the VLP source (see N–S section; Fig. B1c). Therefore, our main conclusion of this paper—that the high-frequency (HF) source location was not identical to the VLP source location—is robust to the assumed Q value.

We also evaluated the effects of an assumed velocity structure on the ASL results. When we used homogeneous velocity structures with $V_p = 2000$ and 3000 m s^{-1}, the results did not change significantly from the case of $V_p = 2500$ m s^{-1}. Note that using $V_p = 2000$ m s^{-1} (3000 m s^{-1}) and $Q = 50$ provides the same

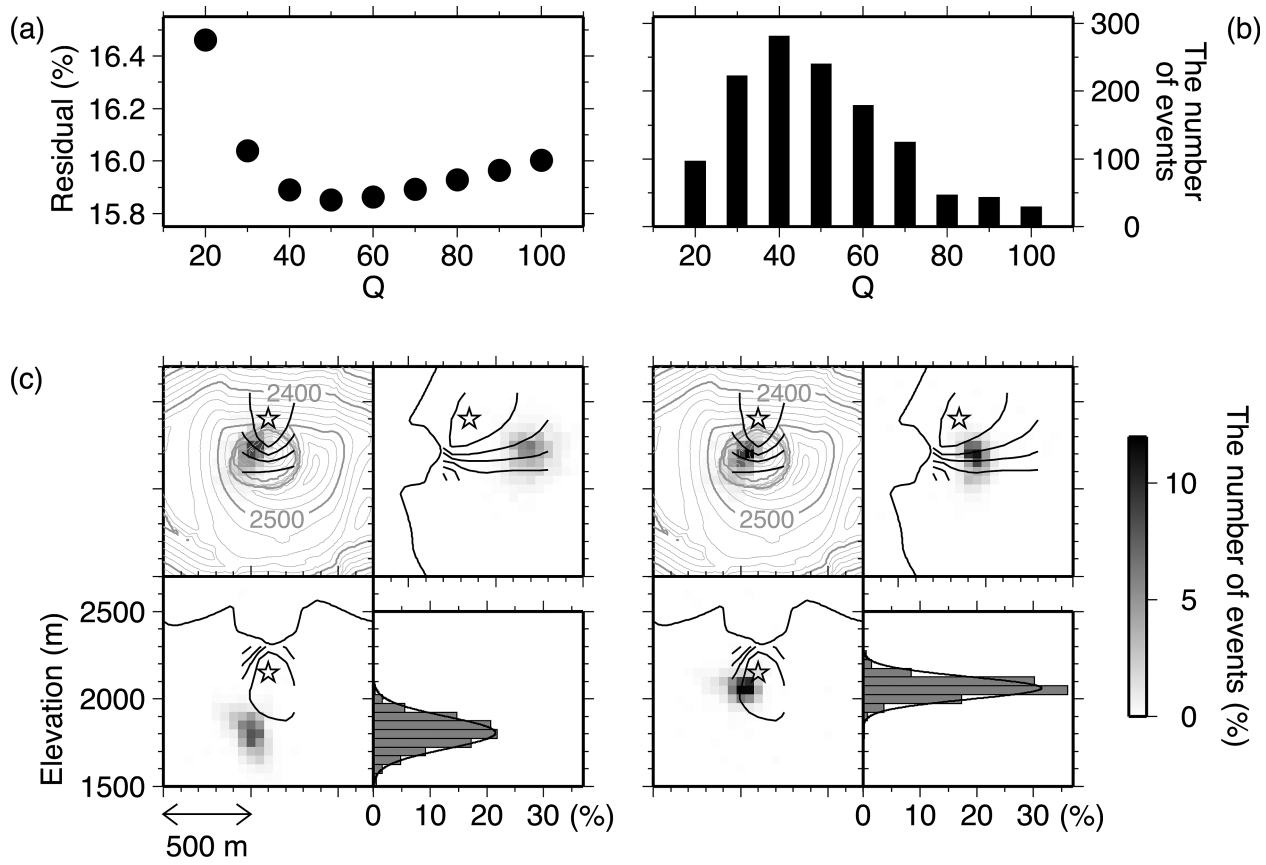

Figure B1. Results of ASL analyses for the 2008–2009 period with various Q values. (a) Residuals between observed and synthetic high-frequency amplitudes averaged over all events for various Q values. (b) The number of events having a minimum residual for each Q value. Note that 169 events of the total of 1437 had a best Q of greater than 100 (omitted from the plot). (c) The numbers of events located at each grid node estimated with $Q = 20$ (left) versus $Q = 100$ (right), using the same format as Fig. 6(a).

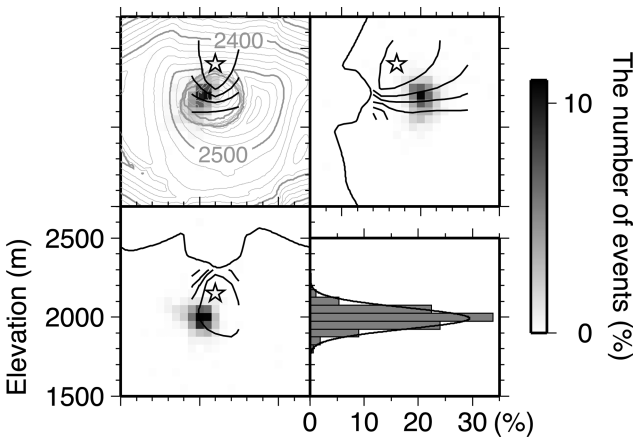

Figure B2. The number of events located at each grid node, plotted using the same format as Fig. 6(a), for the main phase of all VLP events in the 2008–2009 period using a 1-D velocity model based on Aoki *et al.* (2009). In this model, V_p linearly increases with depth from 2000 m s^{-1} at 2500 m above sea level (near the summit) to 4000 m s^{-1} at sea level.

attenuation as using $V_p = 2500$ m s^{-1} and $Q = 40$ (60) (eq. 1). We also used a 1-D velocity structure, with V_p linearly increasing with depth from 2000 m s^{-1} at 2500 m above sea level (near the summit) to 4000 m s^{-1} at sea level. This velocity model is an approximation of Aoki *et al.* (2009) and has been used by waveform inversion by Maeda & Takeo (2011). We used the distance and traveltime along the bending ray for r and T in eq. (1), respectively. The ASLs from this velocity model (Fig. B2) were similar to those from the homogeneous models. In all cases, the HF source locations were deeper than the VLP ones.

APPENDIX C: ASL ANALYSIS USING A THEORETICAL AMPLITUDE EXPRESSION

Morioka *et al.* (2017) theoretically determined that multiple scattering of an S wave would result in a seismic amplitude, given by

$$v = S'_0 \exp\left(-\pi f T / Q_d\right) / r^{0.75}, \quad T = r / V_s, \tag{C1}$$

where S'_0 and Q_d are constants. They point out that this equation (with $Q_d = 17$) gives a distance-amplitude relationship that is close to the one given by eq. (1) (with $Q = 50$). They considered this similarity of the two equations to be a theoretical basis for ASL analysis. Their theory suggests that eq. (C1) would be more appropriate for ASL analysis, although any application of this expression to real data has yet to be reported.

We conducted an ASL analysis based on the theory of Morioka *et al.* (2017) for the main phase of the HF oscillation associated with VLP events at Asama volcano in the 2008–2009 period. We used the same procedure described in the main text, except that we used eq. (C1) with $Q_d = 17$, instead of eq. (1) with $Q = 50$.

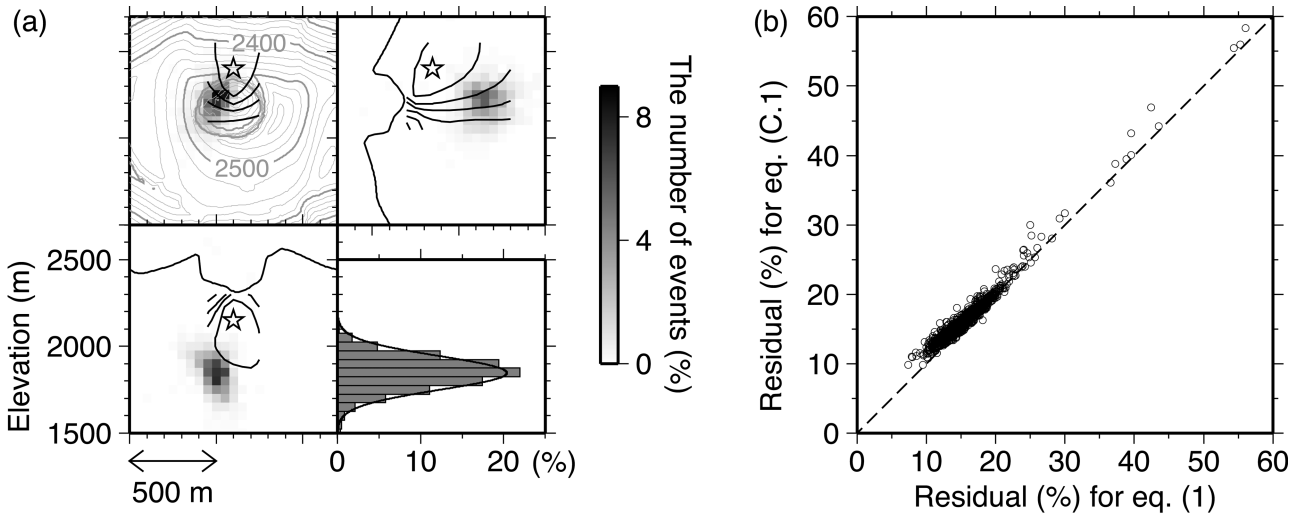

Figure C1. Results of the ASL analysis for the 2008–2009 analysis period based on the theory of Morioka *et al.* (2017). (a) The number of events located at each grid node estimated with eq. (C1) and plotted using the same format as Fig. 6(a). (b) A comparison of the residuals between observed and synthetic amplitudes from the ASL analyses based on eqs (1) (horizontal axis) and (C1) (vertical axis). The two residuals are equal along the dashed line.

Our results (Fig. C1a) indicated that the source elevations estimated with eq. (C1) were systematically deeper than those estimated with eq. (1), whereas horizontal locations of the two estimates were almost identical. The elevations based on eq. (C1) were 1847 (average) ± 97 (standard deviation) m, showing a depth difference of ∼150 m from those based on eq. (1). Theoretically, eq. (C1) should better explain the data; however, residuals between observed and synthetic amplitudes from eq. (C1) were slightly larger than those for eq. (1) for most events (Fig. C1b). We emphasize that our conclusion that the HF source was deeper than the VLP one, remains unchanged, whether we use eq. (C1) or eq. (1).

APPENDIX D: EFFECTS OF SITE AMPLIFICATION FACTORS ON THE ASLs

Walsh *et al.* (2017) showed that site amplification factors may have significant impacts on ASLs. We examined this effect for VLP events at Asama volcano. Following Walsh *et al.* (2017), we generated 1000 random sets of site amplification factors using a Gaussian distribution with the averages and standard deviations given by Table 1 (2008 period). Using each random set, we conducted the ASL analysis for the VLP event shown in Fig. 2. The estimated HF source locations were mostly southwest-downward of the VLP source location (Fig. D1a), showing that our main conclusion does not change by taking into account the errors of the site amplification factors.

We also conducted the ASL analysis for all 571 VLP events in the 2015 period using the site amplification factors in 2011 (Table 1, right). The results (Fig. D1b) were similar to those from the site amplification factors in 2008 (Fig. 6a). We can therefore conclude that the HF source locations are deeper than the VLP ones regardless of which set of the site amplification factors is used.

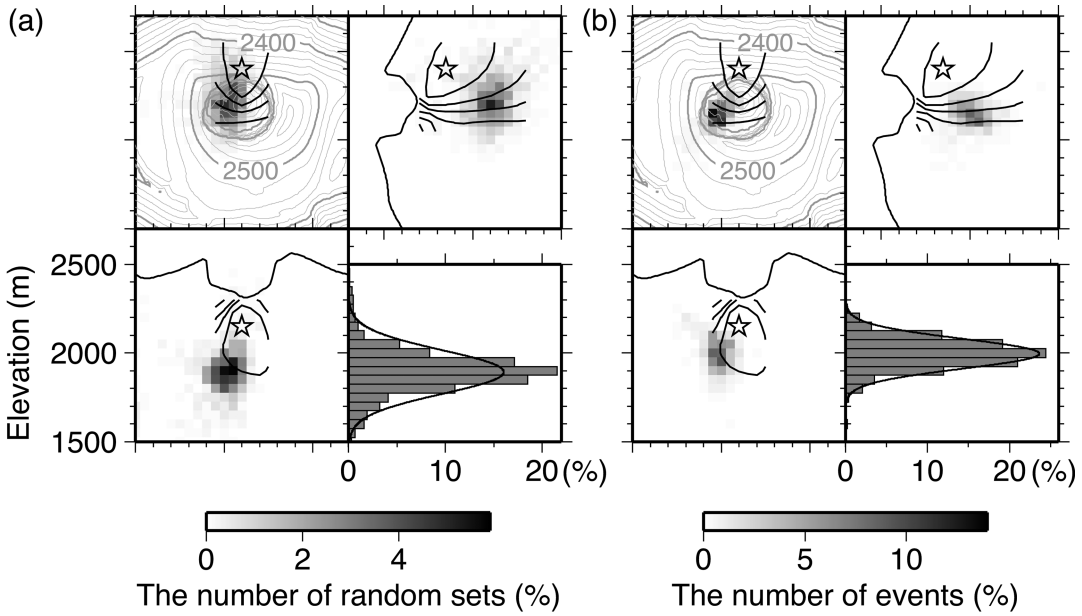

Figure D1. Results of the ASL analysis of the main phase of VLP events from various site amplification factors. (a) Results for a VLP event shown in Fig. 2 from 1000 random sets of site amplification factors generated by a Gaussian distribution based on Table 1 (2008 period; left). The number of random sets from which the event was located at each grid node is shown using the same format as Fig. 6(a). (b) The number of events in the 2015 analysis period located at each grid node from site amplification factors in the 2011 period (Table 1, right).